Vertex-Based Diagrammatic Treatment of Light-Matter-Coupled Systems

Aaram J. Kim,[1] Katharina Lenk,[2] Jiajun Li,[1,3] Philipp Werner,[1] and Martin Eckstein[2]
[1]Department of Physics, University of Fribourg, 1700 Fribourg Switzerland
[2]Department of Physics, University of Erlangen-Nürnberg, 91058 Erlangen, Germany
[3]Paul Scherrer Institute, Condensed Matter Theory, 5352 PSI Villigen, Switzerland

(Received 4 January 2022; accepted 5 December 2022; published 19 January 2023)

We propose a diagrammatic Monte Carlo approach for quantum impurity models, which can be regarded as a generalization of the strong-coupling expansion for fermionic impurity models. The algorithm is based on a self-consistently computed three-point vertex and a stochastically sampled four-point vertex, and it allows one to obtain numerically exact results in a wide parameter regime. The performance of the algorithm is demonstrated with applications to a spin-boson model representing an emitter in a waveguide. As a function of the coupling strength, the spin exhibits a delocalization-localization crossover at low temperatures, signaling a qualitative change in the real-time relaxation. In certain parameter regimes, the response functions of the emitter coupled to the electromagnetic continuum can be described by an effective Rabi model with appropriately defined parameters. We also discuss the spatial distribution of the photon density around the emitter.

DOI: 10.1103/PhysRevLett.130.036901

Introduction.—The optical control of matter has emerged as a promising pathway for tuning material properties. The established paradigm involves disturbing materials with strong lasers [1], leading to exotic nonthermal phases [2–4]. Recently, the enhancement of the coupling between matter and vacuum fluctuations of the electromagnetic field in cavities has been identified as an alternative route for simultaneously engineering matter and light. When photon modes are confined in a near-field cavity or a waveguide, the hybridization between the material and photons can become significantly enhanced, giving rise to novel light-matter phases which exhibit unusual electronic and optical properties [5,6]. Possible applications include controlling the chemical reaction rates through strong collective light-matter coupling [7], while in the solid-state context, experiments have revealed that strong quantum light-matter coupling can enhance ferromagnetism [8], change the robustness of topological phases [9], and possibly affect the critical temperature of unconventional superconductors [10].

A systematic theoretical analysis of these scenarios is challenging. In particular, matter can generically interact with a photon-mode continuum [11,12], such as dispersive waveguide modes [13] which are selectively enhanced by the optical confinement. Ultrastrong coupling between single emitters and an electromagnetic continuum has been experimentally realized in circuit quantum electrodynamics using superconducting qubits [14], and similar physics can be studied by coupling a dipole to quantized surface acoustic waves [15]. Moreover, effective strong coupling may be realized by exploiting excitations which are collectively coupled to both the dipole and photons [16,17]. Previous studies have attacked the problem with polaron transformations [18,19] and matrix-product state simulations [20] for a one-dimensional transmission line cavity. For general cavity setups, perturbative expansions around the high cavity frequency and the infinitely strong coupling limit have been used to go beyond weak-coupling theory [21–23]. However, a theoretical or numerical tool capable of obtaining an unbiased description of matter which is strongly coupled to a photon continuum is still lacking.

In this Letter, we introduce a new diagrammatic approach based on the self-consistent computation of a triangular vertex and the numerical evaluation of a four-point vertex. The algorithm distinguishes itself in several ways from current state-of-the-art algorithms such as weak-coupling diagrammatic expansions [24,25] and the inchworm algorithm [26]. It is based on a strong-coupling expansion, which makes it complementary to the weak-coupling approaches, while the vertex self-consistency goes beyond the inchworm algorithm. This vertex self-consistency significantly improves the convergence toward numerically exact results in the presented examples, and the vertex gives direct access to correlation functions. Combined with the fact that the vertex solver samples connected diagrams in a (two-dimensional) time-stepping procedure, this makes it promising for future nonequilibrium simulations, which typically suffer from a dynamical sign problem. To demonstrate the usefulness of the approach, we apply it to a strongly coupled spin-boson model, representing an emitter in a waveguide. We compute the delocalization-to-localization crossover due to the coupling to a mode continuum, in a regime which is

challenging to explore with exact diagonalization due to the continuum of modes or with matrix product states due to the effect of nonzero temperature.

Model and method.—We consider an infinitely extended rectangular waveguide whose height and width are set to a. A two-level atom is located at position $(a/2, a/2, 0)$ and interacts with the confined photon modes through a dipolar coupling [Fig. 1(a)]. In this geometry, the photon wave numbers along the y and z direction $[k_y \equiv l(\pi/a), k_z \equiv m(\pi/a)]$ are multiples of π/a and will be denoted by (k_l, k_m), while the k_x component can take continuous values up to some cut-off frequency ω_c ($= 30$ eV in the calculations). The waveguide geometry generates a gap $\Omega_{11} = \sqrt{2}c\pi/a$ in the photon spectrum, with c the speed of light. We use the notation $\Omega_{lm}^2 = (k_l^2 + k_m^2)c^2$, so that Ω_{11} denotes the photon energy for the lowest transverse wave number ($l = m = 1$) and vanishing k_x component. In the main text, we only consider the continuum near Ω_{11}.

In the dipolar gauge [27], the Hamiltonian of the atom in the waveguide can be expressed as a spin-boson model, $\hat{\mathcal{H}} = (\Delta/2)\hat{\sigma}_3 + (1/\sqrt{L})\sum_{k\gamma}(g_{k\gamma}\hat{\sigma}_1 a_{k\gamma} + \text{H.c.}) + \sum_{k\gamma}\omega_k a_{k\gamma}^\dagger a_{k\gamma}$, where $\hat{\sigma}_i$ ($i = 1, 2, 3$) denotes the spin-1/2 Pauli operator in the basis of the two matter states, and $a_{k\gamma}^\dagger$ ($a_{k\gamma}$) is the photon creation (annihilation) operator with combined momentum index $k = (k_x, k_y, k_z)$ and (transverse) polarization mode index $\gamma = 1, 2$. L is the length of the waveguide along the x direction. The corresponding bare photon energy is $\omega_k = c\sqrt{k_x^2 + k_y^2 + k_z^2}$. Δ parametrizes the level splitting of the atomic states, and we fix $\Delta = 1.0$ eV. The light-matter coupling is given by $\sum_\gamma |g_{k\gamma}|^2 = (p^2\Omega_{11}^2/\pi\epsilon a^2\omega_k)$, where p is the dipole matrix element for transitions between the two atomic states, and ϵ the vacuum permittivity. By integrating out the photon degrees of freedom [28], one obtains an imaginary-time action for inverse temperature β, $\mathcal{S} = \mathcal{S}_0 - \frac{1}{2}\int_0^\beta d\tau \int_0^\beta d\tau'\, \hat{\sigma}_1(\tau)V(\tau - \tau')\hat{\sigma}_1(\tau')$, where $\mathcal{S}_0$ denotes the local spin action, and $V(\tau) = \sum_{k\gamma}|g_{k\gamma}|^2\mathcal{D}_k^0(\tau)$ is a retarded spin-spin interaction, with the bare k given by $\mathcal{D}_k^0(\tau) = e^{-\omega_k\tau}\theta(-\tau)n_B(\omega_k) + e^{-\omega_k\tau}\theta(\tau)[1 + n_B(\omega_k)]$; n_B denotes the Bose distribution function and $\theta(\tau)$ the Heaviside function.

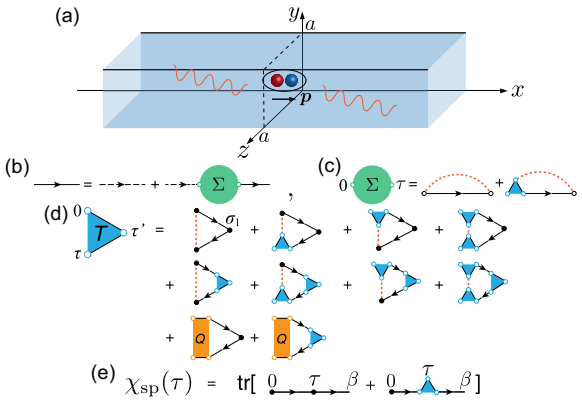

FIG. 1. (a) Schematic picture of the rectangular waveguide with width a in both the y and z direction. The electric dipole with moment $\boldsymbol{p} = p\hat{\sigma}_1\mathbf{e}_x$ along the x direction is located at $(0, a/2, a/2)$. (b)–(e) Diagrammatic hierarchy between the triangular and four-point vertex, the self-energy, the Green's function, and the spin correlation function related via (b) the Dyson equation, (c) the Schwinger-Dyson equation, (d) the vertex self-consistency equation, and (e) the equation for the spin-correlation function. The dashed lines present the effective spin interaction $V(\tau - \tau')$, and solid (dashed) arrows show the (bare) local propagator $\hat{\mathcal{G}}$ ($\hat{\mathcal{G}}_0$). The solid dot denotes the Pauli matrix $\hat{\sigma}_1$, and the open dots emphasize the encapsulated $\hat{\sigma}_1$ in the triangular and four-point vertex.

The solution of the model is formulated in terms of the resolvent operator (or pseudoparticle propagator) $\hat{\mathcal{G}}(\tau) = \text{tr}_{\text{ph}}\{\mathcal{T}_\tau \exp[-\int_0^\tau d\tau' \hat{H}(\tau')]\}$ in imaginary time ($0 \le \tau \le \beta$), which is a 2×2 matrix in matter space after the partial trace over the photon degrees of freedom. Starting from the noninteracting propagator $\hat{\mathcal{G}}_0(\tau) = e^{-(\Delta/2)\hat{\sigma}_3\tau}$, a systematic diagrammatic perturbation in the retarded spin-spin interaction $V(\tau)$ can be written down in terms of a self-energy correction $\hat{\Sigma}(\tau)$ and the time-ordered Dyson equation $\hat{\mathcal{G}}(\tau) = \hat{\mathcal{G}}_0(\tau) + \int_0^\tau d\tau_2 \int_0^{\tau_2} d\tau_1 \hat{\mathcal{G}}_0(\tau - \tau_2)\hat{\Sigma}(\tau_2 - \tau_1)\hat{\mathcal{G}}(\tau_1)$ [Fig. 1(b)]. The exact self-energy is given by the sum of the leading term $\hat{\Sigma}_{\text{NCA}}(\tau) = V(\tau)\hat{\sigma}_1\hat{\mathcal{G}}(\tau)\hat{\sigma}_1$, called the noncrossing approximation (NCA) [29], and the vertex correction $\hat{\Sigma}_v(\tau) = \int_0^\tau d\tau_1 \int_{\tau_1}^\tau d\tau_2 \hat{\mathcal{G}}(\tau - \tau_2)V(\tau - \tau_1)\hat{T}(\tau_2, \tau_1)$ [Fig. 1(c)]. Here the three-point vertex $\hat{T}(\tau_2, \tau_1)$ sums up all diagrams with interaction lines dressing the operator $\hat{\sigma}_1$; it can be represented in terms of a self-consistent set of exact diagrammatic equations, as illustrated in Fig. 1(d). In the figure, the (orange) square is the four-point vertex $Q(\tau; \tau_2, \tau_1)$, which is one-particle irreducible in the interaction line and two-particle irreducible in the local time-evolution operator. The triangular vertex equation must be solved self-consistently with the Dyson equation for $\hat{\Sigma}$. To compute the Q vertex, we developed a diagrammatic Monte Carlo (DiagMC) scheme [30–32], which stochastically samples all possible Feynman diagrams of the Q vertex (for details, see Ref. [33]). Upon convergence with diagram order, the addition of the Q vertex in the self-consistency equation for $\hat{T}$ guarantees a numerically exact solution. Finally, relevant observables are evaluated in terms of $\hat{\mathcal{G}}$ and $\hat{T}$; in particular, the exact spin-correlation function $\chi_{\text{sp}} = \langle\hat{\sigma}_1(\tau)\hat{\sigma}_1(0)\rangle$ is given by

$$\chi_{\text{sp}}(\tau) = \frac{1}{Z}\text{tr}[\hat{\mathcal{G}}(\beta - \tau)\hat{\sigma}_1\hat{\mathcal{G}}(\tau)\hat{\sigma}_1] + \frac{1}{Z}\int_0^\tau d\tau_1 \int_\tau^\beta d\tau_2 \times \text{tr}[\hat{\mathcal{G}}(\beta - \tau_2)\hat{T}(\tau_2 - \tau_1, \tau - \tau_1)\hat{\mathcal{G}}(\tau_1)\hat{\sigma}_1], \quad (1)$$

with $Z = \mathrm{tr}[\hat{\mathcal{G}}(\beta)]$ [Fig. 1(e)]. While we focus here on the spin-boson model, the vertex formalism introduced here can be extended to general impurity models with fermionic or bosonic bath degrees of freedom [33].

Below we will denote by Q_n the fully self-consistent approximation which includes the four-point vertex up to order n; Q_0 is also referred to as the triangular vertex approximation (TVA). We will also compare this to simpler schemes which do not involve the four-point vertex [28], in particular the NCA approximation $\hat{\Sigma} \approx \hat{\Sigma}_{\mathrm{NCA}}$; the one-crossing approximation (OCA) [34], which approximates $\hat{T}$ by the first diagram in Fig. 1(d); the two-crossing approximation (TCA) which keep self-energy diagrams with one and two crossings of the interaction lines; and the third-order approximation, which keeps all self-energy diagrams up to the third order.

As a first test of the solver, we consider the model with only a single photon mode, for which the spin-correlation function $\chi_{\mathrm{sp}} = \langle \hat{\sigma}_1(\tau)\hat{\sigma}_1(0)\rangle$ can be calculated by exact diagonalization. In Fig. 2(a), one can see that the exact result (dashed line) is recovered for a sufficiently high ($\gtrsim$10) diagram order in Q. Figure 2(c) shows that the applied vertex self-consistency (red crosses) considerably improves the results compared to schemes without it, like

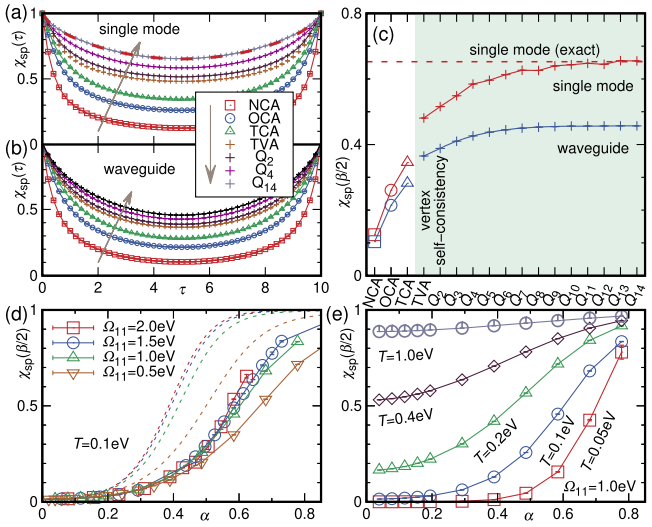

FIG. 2. Spin-correlation function $\chi_{\mathrm{sp}}(\tau)$ for the approximate schemes (NCA, OCA, TCA, TVA) and the Monte Carlo simulation including the Q-vertex diagrams to order n (labeled Q_n). (a) Single-mode benchmark with $T = 0.1$ eV, $g = 1.4$ eV, and $\omega = 1.5$ eV; (b) Waveguide with $T = 0.1$ eV, $p = 3$ eμm, and $\Omega_{11} = 1.0$ eV. The red dashed line in (a) presents the exact diagonalization result for the benchmark. (c) Systematic convergence of $\chi_{\mathrm{sp}}(\beta/2)$ with diagram order. (d) and (e) Converged spin correlation functions for the waveguide model at $\tau = \beta/2$ as a function of the coupling strength α, and for various temperatures at fixed photon gap $\Omega_{11} = 1.0$ eV (e), for various photonic gap sizes at a fixed temperature $T = 0.1$ eV (d). Dashed lines in (d) show the results for the effective single-mode cavity model.

NCA, OCA, and TCA. This promising feature of the vertex impurity solver distinguishes it from other state-of-the-art algorithms such as the inchworm algorithm [26], which are based on a self-energy sampling without vertex self-consistency.

Results.—We now turn to the waveguide problem with continuous bath degrees of freedom, which cannot be solved with exact diagonalization. The chosen parameter set ($T = 0.1$ eV, $p = 3$ eμm, and $\Omega_{11} = 1.0$ eV) represents the most challenging regime, where all energy scales are comparable. (For specific applications such as superconducting qubits [14], one would simply have to rescale the energy unit.) Convergence to the exact result can be achieved by sampling the Q vertex up to order 14. The blue crosses in Fig. 2(c) illustrate the systematic convergence of χ_{sp} as a function of diagram order of the Q vertex. As in the single-mode case, the vertex self-consistency improves the accuracy, and the corrections from the Q vertex are essential for reliable results in this strong-coupling regime.

At low but nonzero temperatures, the atom in the waveguide exhibits a crossover from a fluctuating state to a polarized state with increasing coupling strength, which we parametrize with the dimensionless constant $\alpha^2 = p^2\Omega_{11}^2/2\epsilon\pi^3c^3$. α^2 controls the induced interaction strength from the lowest-energy photon mode, $\frac{1}{c\Omega_{11}}\sum_\gamma g^2_{k_x=0,\gamma}$, which is empirically found to be useful even in the continuum case. For a given energy unit Δ, it is sufficient to explore the α dependence of the system for various Ω_{11}. Figures 2(d) and 2(e) show the converged $\chi_{\mathrm{sp}}(\beta/2)$, a measure for the localization of the dipole, as a function of α. Figure 2(e) plots $\chi(\beta/2)(\alpha)$ for different temperatures and a fixed photonic gap. As we enhance the quantum coherence by decreasing the temperature, $\chi_{\mathrm{sp}}(\beta/2)$ is considerably suppressed in the weak-coupling regime ($\alpha \lesssim 0.4$). In the strong-coupling regime χ_{sp} shows a slow decay at long times, indicating a localized spin in the x direction. The crossover defined by the inflection point of $\chi_{\mathrm{sp}}(\beta/2)$ gradually shifts to stronger couplings α, and the crossover becomes sharper as we decrease the temperature. In contrast to previous studies of the spin-boson model with a gapless Ohmic bath [35], $V(\tau)$ decays faster than τ^{-2}, and we do not expect a localization transition at zero temperature [36].

For a fixed nonzero temperature, the $\chi_{\mathrm{sp}}(\beta/2)$ data for various photonic gap sizes collapse onto a single curve in the weak coupling regime [Fig. 2(d)], when plotted as a function of the dimensionless parameter α. In the crossover regime, the χ_{sp} curves for different gap sizes start to disperse; the larger the gap size, the lower the crossover point in terms of α. The data, however, indicate a nontrivial crossover to a localized state in the limit $\Omega_{11} \to \infty$, where the photonic gap is much larger than the level splitting. This is because of the increasing light-matter coupling strength with increasing photonic gap (decreasing width of the waveguide).

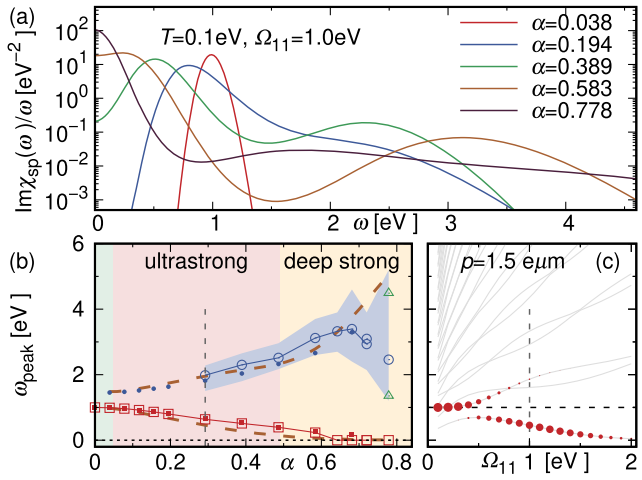

FIG. 3. (a) Spin relaxation function $\mathrm{Im}\chi_{\mathrm{sp}}(\omega)/\omega$ for various coupling strengths α, analytically continued by MaxEnt. (b) Peak locations of the lower and upper polariton modes obtained by Padé (solid symbols) and MaxEnt (open symbols), with the full width at half maximum indicated by the blue shading. Brown dashed lines show the relevant excitation energies in the effective Rabi model; for the given parameters, the couplings are $g_{\mathrm{eff}} = 2.86\Omega_{11}\alpha$ and $\omega_{\mathrm{eff}} = 1.4\Omega_{11}$. (c) Spectrum of the effective Rabi model, for $p = 1.5$ eμm as a function of Ω_{11}. For $\Omega_{11} = 1$ eV, the corresponding $\alpha = 0.292$, see vertical line in panel (b). The symbol size is proportional to the contribution of the excitation to $\chi_{\mathrm{sp}}(\omega)$.

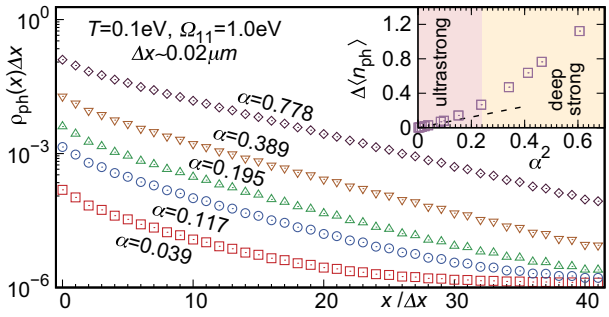

FIG. 4. Spatial distribution of the photon density $\rho_{\mathrm{ph}}(x)$ as a function of the distance x to the dipole, for various coupling strengths α. The inset shows the total bound photon number as a function of the coupling α.

Figure 3(a) presents the spin relaxation function $\mathrm{Im}\chi_{\mathrm{sp}}(\omega)/\omega$. Real frequency data have to be obtained by an analytical continuation of $\chi_{\mathrm{sp}}(\tau)$. We compare two complementary analytic continuation methods, the maximum entropy (MaxEnt) method [37,38] and the Padé approximation [39], in order to approximately estimate the uncertainty in the peak positions [28]. Without the waveguide, the result would be a delta function at $\omega = 1$ eV (broadened by MaxEnt). The spin-photon coupling splits the spin excitation into two separate polariton modes. The lower polariton mode shifts to $\omega \to 0$ as we increase α, while the upper polariton mode moves to higher energy. As expected, the upper polariton mode is suppressed at higher energies, but its peak height strongly depends on the photonic gap [28]. The width of the high-energy satellite increases with increasing α, and for $\alpha \gtrsim 0.6$ it becomes difficult to pinpoint the peak location within the numerical accuracy of analytic continuation. In the same strong coupling regime, the two low-energy peaks at positive and negative energy start to merge, resulting in a single peak at $\omega = 0$. This signals a qualitative change in the relaxation dynamics of the spin in real time, $\langle\hat{\sigma}_1(t)\rangle$, for a polarized initial condition $\langle\hat{\sigma}_1(0)\rangle = 1$. In the case of a two-peak spectrum, the spin shows an underdamped oscillation, while it exhibits an overdamped relaxation in the single-peak case.

The splitting of the excitation spectrum into upper and lower polaritons looks similar to a conventional Rabi model, where a two-level emitter is coupled to a single cavity mode, even though the situation in the present case is very different, and for the parameters of Fig. 3, the bare excitation energy Δ is located right at the edge of a continuum. Upon increasing the light-matter coupling, the lower polariton is pushed into the photonic gap (but still remains damped), while the upper polariton overlaps with the photon continuum. Nevertheless, the retarded interaction $V(\tau)$ suggests a way to construct an effective Rabi model with photon energy ω_{eff} and light-matter coupling g_{eff}, which can provide insights into the polariton splitting. We determine the two effective parameters by identifying the retarded interaction $V(\tau)$ of the waveguide model with $V_{\mathrm{eff}}(\tau) = g_{\mathrm{eff}}^2 \cosh[(\tau - \beta/2)\omega_{\mathrm{eff}}]/\sinh(\beta\omega_{\mathrm{eff}}/2)$ of the effective model at $\tau = 0$ and $\beta/2$. The detailed dependence of ω_{eff} and g_{eff} on α and Ω_{11} is analyzed in the Supplemental Material [28]. In particular, in the low temperature limit $\beta\Omega \gg 1$, we have $\omega_{\mathrm{eff}} \approx \Omega_{11}$, and $g_{\mathrm{eff}}^2 \approx 2\alpha^2\Omega_{11}^2 \log(2\omega_c/\Omega_{11})$, so that up to a logarithmic dependence in the high-energy cutoff $\alpha \sim g_{\mathrm{eff}}/\omega_{\mathrm{eff}}$ is related to the conventional dimensionless coupling in the Rabi model.

In Fig. 3(c), we show the excited states of the Rabi model with $n_{\mathrm{ph}} \leq 1$ photons, and their contribution to $\chi_{\mathrm{sp}}(\omega)$ as a function of Ω_{11} at fixed p. One can see that the lower polariton mode becomes the dominant spin excitation in the narrow waveguide with $\Omega_{11} > \Delta$. It is renormalized toward zero for large Ω_{11}, because of the increase of g_{eff} with Ω_{11}. Finally, the brown dashed lines in Fig. 3(b) show the two leading excitation energies in the resulting Rabi model, which fit the exact behavior remarkably well. This shows that the effective Rabi model provides a meaningful estimate of the coupling to a continuum, at least in the regime where the bare mode is not overlapping with the continuum. For a smaller value of Ω_{11}, see the Supplemental Material [28].

The spin-photon coupling also renormalizes the photon propagator via the equation of motion, $\mathcal{D}_{k\gamma,k'\gamma'}(iq_n) = \delta_{\gamma\gamma'}\delta_{kk'}\mathcal{D}^0_k(iq_n) - (g_{k\gamma}g_{k'\gamma'}/L)\mathcal{D}^0_k(iq_n)\chi_{\mathrm{sp}}(iq_n)\mathcal{D}^0_{k'}(iq_n)$, resulting in a photon bound state centered at the dipole. Figure 4 shows the spatial distribution of the photon density

$\rho_{\mathrm{ph}}(x)$ in the vicinity of the spin for various coupling strengths α, and the total bound photon density $\Delta\langle n_{\mathrm{ph}}\rangle = \int dx[\rho_{\mathrm{ph}}(x) - \rho_0]$, where ρ_0 is the noninteracting photon density due to thermal excitations. One can see that the photon distribution decays exponentially to the thermal background, and $\Delta\langle n_{\mathrm{ph}}\rangle$ becomes of order 1 in the deep strong coupling limit ($\alpha \gtrsim 0.49$).

Conclusions.—We have introduced a vertex-based diagrammatic algorithm which allows one to study strong light-matter coupling problems in the presence of a continuum of photon modes, and demonstrated its effectiveness with applications to the spin-boson model with coupling strength comparable to the cavity frequency and level splitting. The boldified [40–48] DiagMC method [30–32] has been reformulated to directly sample the four-point vertex with nonlocal-in-time interactions in pseudoparticle space [49,50]. The self-consistency at the level of the triangular vertex improves the approximation at a given diagram order, and speeds up the convergence to the exact results. While a self-consistent series in general can suffer from the multivaluedness problem [33,51–61], this does not seem to be the case for the present situation [28].

With modified local propagators, the method can also be applied to the Anderson impurity model and related impurity problems with relevance for dynamical mean field theory. In this context, our method provides a systematic path for high-order, self-consistent *strong-coupling* expansions. While in equilibrium, alternative powerful Monte Carlo methods exist [62,63], the new approach introduced here is promising also for nonequilibrium applications, which will be the subject of forthcoming studies.

This work was supported by ERC Consolidator Grant No. 724103 (A. J. K., P. W.), by SNSF Grant No. 200021-196966, and the Marie Skłodowska Curie Grant Agreement No. 884104 (PSI-FELLOW-III-3i) (J. L.). K. L. and M. E. were funded by the ERC Starting Grant No. 716648, and by the Deutsche Forschungsgemeinschaft (DFG, German Research Foundation)—Project-ID No. 429529648—TRR 306 QuCoLiMa ("Quantum Cooperativity of Light and Matter"). The calculations have been performed on the Beo05 cluster at the University of Fribourg.

[1] D. N. Basov, R. D. Averitt, and D. Hsieh, Nat. Mater. **16**, 1077 (2017).
[2] D. Fausti, R. I. Tobey, N. Dean, S. Kaiser, A. Dienst, M. C. Hoffmann, S. Pyon, T. Takayama, H. Takagi, and A. Cavalleri, Science **331**, 189 (2011).
[3] J. W. McIver, B. Schulte, F. U. Stein, T. Matsuyama, G. Jotzu, G. Meier, and A. Cavalleri, Nat. Phys. **16**, 38 (2020).
[4] H. Yamakawa, T. Miyamoto, T. Morimoto, N. Takamura, S. Liang, H. Yoshimochi, T. Terashige, N. Kida, M. Suda, H. M. Yamamoto, H. Mori, K. Miyagawa, K. Kanoda, and H. Okamoto, Nat. Commun. **12**, 953 (2021).
[5] A. Frisk Kockum, A. Miranowicz, S. De Liberato, S. Savasta, and F. Nori, Nat. Rev. Phys. **1**, 19 (2019).
[6] P. Forn-Díaz, L. Lamata, E. Rico, J. Kono, and E. Solano, Rev. Mod. Phys. **91**, 025005 (2019).
[7] T. W. Ebbesen, Acc. Chem. Res. **49**, 2403 (2016).
[8] A. Thomas, E. Devaux, K. Nagarajan, G. Rogez, M. Seidel, F. Richard, C. Genet, M. Drillon, and T. W. Ebbesen, Nano Lett. **21**, 4365 (2021).
[9] F. Appugliese, J. Enkner, L. Paravicini-Bagliani Gian, M. Beck, C. Reichl, W. Wegscheider, G. Scalari, C. Ciuti, and J. Faist, Science **375**, 1030 (2022).
[10] A. Thomas, E. Devaux, K. Nagarajan, T. Chervy, M. Seidel, D. Hagenmüller, S. Schütz, J. Schachenmayer, C. Genet, G. Pupillo, and T. W. Ebbesen, arXiv:1911.01459.
[11] A. S. Sheremet, M. I. Petrov, I. V. Iorsh, A. V. Poshakinskiy, and A. N. Poddubny, arXiv:2103.06824.
[12] P. Forn-Díaz, J. J. García-Ripoll, B. Peropadre, J. L. Orgiazzi, M. A. Yurtalan, R. Belyansky, C. M. Wilson, and A. Lupascu, Nat. Phys. **13**, 39 (2017).
[13] V. Rokaj, M. Ruggenthaler, F. G. Eich, and A. Rubio, Phys. Rev. Res. **4**, 013012 (2022).
[14] A. Blais, R.-S. Huang, A. Wallraff, S. M. Girvin, and R. J. Schoelkopf, Phys. Rev. A **69**, 062320 (2004).
[15] R. Manenti, A. F. Kockum, A. Patterson, T. Behrle, J. Rahamim, G. Tancredi, F. Nori, and P. J. Leek, Nat. Commun. **8**, 975 (2017).
[16] S. Schütz, J. Schachenmayer, D. Hagenmüller, G. K. Brennen, T. Volz, V. Sandoghdar, T. W. Ebbesen, C. Genes, and G. Pupillo, Phys. Rev. Lett. **124**, 113602 (2020).
[17] D. Sidler, C. Schäfer, M. Ruggenthaler, and A. Rubio, J. Phys. Chem. Lett. **12**, 508 (2021).
[18] G. Díaz-Camacho, A. Bermudez, and J. J. García-Ripoll, Phys. Rev. A **93**, 043843 (2016).
[19] T. Shi, Y. Chang, and J. J. García-Ripoll, Phys. Rev. Lett. **120**, 153602 (2018).
[20] E. Sanchez-Burillo, D. Zueco, J. J. Garcia-Ripoll, and L. Martin-Moreno, Phys. Rev. Lett. **113**, 263604 (2014).
[21] F. Schlawin, A. Cavalleri, and D. Jaksch, Phys. Rev. Lett. **122**, 133602 (2019).
[22] J. Li, L. Schamriß, and M. Eckstein, Phys. Rev. B **105**, 165121 (2022).
[23] Y. Ashida, T. Yokota, A. Imamoglu, and E. Demler, arXiv:2105.08833.
[24] R. E. V. Profumo, C. Groth, L. Messio, O. Parcollet, and X. Waintal, Phys. Rev. B **91**, 245154 (2015).
[25] M. Maček, P. T. Dumitrescu, C. Bertrand, B. Triggs, O. Parcollet, and X. Waintal, Phys. Rev. Lett. **125**, 047702 (2020).
[26] G. Cohen, E. Gull, D. R. Reichman, and A. J. Millis, Phys. Rev. Lett. **115**, 266802 (2015).
[27] J. Li, D. Golez, G. Mazza, A. J. Millis, A. Georges, and M. Eckstein, Phys. Rev. B **101**, 205140 (2020).
[28] See Supplemental Material at http://link.aps.org/supplemental/10.1103/PhysRevLett.130.036901 for the technical details of the diagrammatic methods, the waveguide setup, the photonic-gap dependence of the spin excitation, the analysis of the effective Rabi model, the numerical analytic continuation methods, and the multivaluedness problem.

[29] H. Keiter and J. C. Kimball, Int. J. Magn. **1**, 233 (1971).
[30] N. V. Prokof'ev and B. V. Svistunov, Phys. Rev. Lett. **81**, 2514 (1998).
[31] K. Van Houcke, E. Kozik, N. Prokof'ev, and B. Svistunov, Phys. Procedia **6**, 95 (2010).
[32] E. Kozik, K. Van Houcke, E. Gull, L. Pollet, N. Prokof'ev, B. V. Svistunov, and M. Troyer, Europhys. Lett. **90**, 10004 (2010).
[33] A. J. Kim, J. Li, M. Eckstein, and P. Werner, Phys. Rev. B **106**, 085124 (2022).
[34] T. Pruschke and N. Grewe, Z. Phys. B **74**, 439 (1989).
[35] A. J. Leggett, S. Chakravarty, A. T. Dorsey, M. P. A. Fisher, A. Garg, and W. Zwerger, Rev. Mod. Phys. **59**, 1 (1987).
[36] J. Fröhlich and T. Spencer, Commun. Math. Phys. **84**, 87 (1982).
[37] R. K. Bryan, Eur. Biophys. J. **18**, 165 (1990).
[38] M. Jarrell and J. E. Gubernatis, Phys. Rep. **269**, 133 (1996).
[39] H. J. Vidberg and J. W. Serene, J. Low Temp. Phys. **29**, 179 (1977).
[40] N. Prokof'ev and B. Svistunov, Phys. Rev. Lett. **99**, 250201 (2007).
[41] N. V. Prokof'ev and B. V. Svistunov, Phys. Rev. B **77**, 125101 (2008).
[42] K. Van Houcke, F. Werner, E. Kozik, N. Prokof'ev, B. Svistunov, M. J. H. Ku, A. T. Sommer, L. W. Cheuk, A. Schirotzek, and M. W. Zwierlein, Nat. Phys. **8**, 366 (2012).
[43] A. S. Mishchenko, N. Nagaosa, and N. Prokof'ev, Phys. Rev. Lett. **113**, 166402 (2014).
[44] Y. Deng, E. Kozik, N. V. Prokof'ev, and B. V. Svistunov, Europhys. Lett. **110**, 57001 (2015).
[45] R. Rossi, T. Ohgoe, K. Van Houcke, and F. Werner, Phys. Rev. Lett. **121**, 130405 (2018).
[46] R. Rossi, T. Ohgoe, E. Kozik, N. Prokof'ev, B. Svistunov, K. Van Houcke, and F. Werner, Phys. Rev. Lett. **121**, 130406 (2018).
[47] K. Van Houcke, F. Werner, T. Ohgoe, N. V. Prokof'ev, and B. V. Svistunov, Phys. Rev. B **99**, 035140 (2019).
[48] K. Van Houcke, F. Werner, and R. Rossi, Phys. Rev. B **101**, 045134 (2020).
[49] S. E. Barnes, J. Phys. F **6**, 1375 (1976).
[50] P. Coleman, Phys. Rev. B **29**, 3035 (1984).
[51] E. Kozik, M. Ferrero, and A. Georges, Phys. Rev. Lett. **114**, 156402 (2015).
[52] R. Rossi and F. Werner, J. Phys. A **48**, 485202 (2015).
[53] T. Schäfer, S. Ciuchi, M. Wallerberger, P. Thunström, O. Gunnarsson, G. Sangiovanni, G. Rohringer, and A. Toschi, Phys. Rev. B **94**, 235108 (2016).
[54] R. Rossi, F. Werner, N. Prokof'ev, and B. Svistunov, Phys. Rev. B **93**, 161102(R) (2016).
[55] O. Gunnarsson, G. Rohringer, T. Schäfer, G. Sangiovanni, and A. Toschi, Phys. Rev. Lett. **119**, 056402 (2017).
[56] P. Thunström, O. Gunnarsson, S. Ciuchi, and G. Rohringer, Phys. Rev. B **98**, 235107 (2018).
[57] P. Chalupa, P. Gunacker, T. Schäfer, K. Held, and A. Toschi, Phys. Rev. B **97**, 245136 (2018).
[58] A. J. Kim and V. Sacksteder, Phys. Rev. B **101**, 115146 (2020).
[59] A. J. Kim, P. Werner, and E. Kozik, arXiv:2012.06159.
[60] M. Reitner, P. Chalupa, L. Del Re, D. Springer, S. Ciuchi, G. Sangiovanni, and A. Toschi, Phys. Rev. Lett. **125**, 196403 (2020).
[61] K. Van Houcke, E. Kozik, R. Rossi, Y. Deng, and F. Werner, arXiv:2102.04508.
[62] P. Werner, A. Comanac, L. de' Medici, M. Troyer, and A. J. Millis, Phys. Rev. Lett. **97**, 076405 (2006).
[63] M. Weber, Phys. Rev. B **105**, 165129 (2022).